Experimental mesoscopic investigation of the local cyclic plasticity of a non-oriented electrical steel

Jeremie Bouquerel, C. Schayes, Jean-Bernard Vogt

Experimental mesoscopic investigation of the local cyclic plasticity of a non-oriented electrical steel

J. Bouquerel*, C. Schayes, J.B. Vogt

Univ. Lille, CNRS, INRAE, Centrale Lille, UMR 8207 -
UMET - Unité Matériaux et Transformations, F-59000 Lille, France

*Corresponding author : jeremie.bouquerel@centralelille.fr

Abstract

Complementary mesoscopic investigations have been carried out on a notched specimen, made of Fe-3%Si steel and submitted to fatigue loading. Load control fatigue testing was conducted to ensure localised cyclic deformation and the resulting displacement fields were measured by means of Digital Image Correlation (DIC). Electron Channelling Contrast Imaging (ECCI) and Electron Back-Scatter Diffraction (EBSD) complete the DIC data by giving a different view of the local plasticity, as they image the dislocation structure and map their related characteristics, such as misorientation.

Hence, two misorientation based criteria, namely Grain Reference Orientation Deviation (GROD) and Grain Orientation Spread (GOS) were considered for EBSD analysis. Based on a previous study, a <GOS> – $\Delta\varepsilon_t$ abacus has been coupled with a <GOS> - DIC abacus in order to evaluate locally the encountered strain field and link this latter to an equivalent total strain variation. The obtained results have been discussed from the evolution of the dislocations structures, as observed by ECCI.

This combination of mesoscopic techniques clearly emphasizes the local deformation by means of both qualitative and quantitative measurements. On one hand, DIC and EBSD measurements indicate the presence of strain localisation which can be correlated to a certain level of cyclic strain amplitude. On the other hand, the variation of the strain levels and its distribution when moving away from the notch are confirmed by the dislocation structures evolution seen by ECCI. Such

structures vary from cells, vein and channels and entangled dislocations regions as the analysed areas go away from the notch.
At a local scale, the DIC measurements behave as numerous virtual extensometers while its combination with EBSD and ECCI data confirms the correlation with the accumulated cyclic strain.

1. Introduction

Nowadays, the knowledge and the understanding of the plasticity phenomena remain fantastic challenges for both engineers and researchers. On one hand, it allows the design of materials and/or components that exhibit superior mechanical properties by optimising their microstructure and by improving thermomechanical treatments to which those latter are submitted. On the other hand, it allows a lifetime optimisation as materials may undergo various types of constraints when in operating conditions.

One of the constraints which has a high occurrence concerns the fatigue loading, which can be related to expected or unexpected in-service conditions. Indeed, fatigue corresponds to the progressive and structural damage that occurs when a material is subjected to cyclic loading. It is a major cause of component failure in many industrial domains such as construction [1,2], energy [3–5] and transportation [6–10].

The Fe-3%Si steel (M330-35A) is of prime interest in regards with the industrial sectors mentioned above. As it belongs to the non-oriented electrical steels, it is frequently used for its electrotechnical properties obtained by a well-controlled combination of chemical composition, grain-based features (morphologic and crystallographic texture) and sheet thickness (350 µm). It is then particularly adapted to rotating machines such as alternators.

This steel and more generally the iron-silicon electrical steels have been specifically optimised for their electrical properties and more precisely for the prediction of core losses to improve electrical machine design [11–14], but less their mechanical properties. Nevertheless, the rotor design

improvement requires now to clearly know their mechanical properties and more precisely their fatigue properties.

Within the last decades, metallurgists and mechanical engineers have developed robust characterisation tools to characterise the plastic deformation that occurs during fatigue. Although the synergies and tools were initially different, the frontier between their approaches become more and more narrow. Indeed, metallurgists pay more attention to microstructural developments ranging from more or less complex dislocation interactions to more mesoscopic misorientation build-up. To their side, the mechanical community evaluated deformation in terms of stresses and strains and part of them are focusing on microstructural impact through micromechanics.

Several interesting tools may then be considered for investigations at the mesoscopic and macroscopic scales. Electron Back-Scatter Diffraction (EBSD) and Electron Contrast Channelling Imaging (ECCI) bring valuable information regarding deformation as it can be viewed from microstructural evolution. Digital Image Correlation (DIC) gives quantitative data regarding the strain and stress field at various scales. Finally, simulation based on Finite Element Modelling (FEM), arises to predict or validate materials and component behaviours.

All those techniques take benefits from a constant development brought from their respective community, which give a more precise ability for the plastic deformation analysis [15–24]. When regarding their applications to fatigue behaviour, those approaches are often used separately [25–27], although few recent works tried to perform some correlation [24,28–31]. However, only a fragmentary view of the material characteristics is treated in order to describe mechanisms related to crack initiation or first steps of crack propagation by focusing on.

The purpose of the present work is somehow different. Two previous studies performed on the fatigue behaviour of the M330-35A steel point out the ability of EBSD and ECCI to give mesoscopic details allowing the explanation of the stress response of the material to strain cycling [32,33]. It was also shown that, depending on the applied strain, this steel exhibits behaviours corresponding to low

temperature and high temperature regimes. Moreover, EBSD based criteria pointed out the associated strain localisation that leads to crack initiation. In the present study, those results are used as a kind of abacus in order to estimate the fatigue strain encountered during the cyclic loading of a notched sample. The comparison between the SEM based analysis and the DIC measurements validates the previous approach on a sample with a more complex shape, for which both stress and strain distribution is heterogeneous. Mesoscopic DIC measurements gives a large amount of local virtual extensometers for the different areas of the sample, while EBSD/ECCI confirm the encountered strain levels assess the presence of dislocations cells.

2. Material and experimental procedure

2.1. Material

The material considered in this study is the M330-35A of the EN10106 classification (or graded as 36F185 according to ASTM A677). This corresponds to a non-oriented silicon steel with the chemical composition given in Table 1.

Table 1: Chemical composition of the M330-35A steel (wt%)

Elements	C	Mn	P	Si	S	Al	Fe
wt%	0.003	0.109	0.011	2.884	0.004	0.448	Bal.

The material has been provided in thin sheet, 350 µm in thickness, but no details regarding the rolling conditions have been given by the supplier. It exhibits a ferritic structure (Figure 1) with a wide grain size distribution [32–34]. The average grain size determined by the intercept method is 75 µm. The sheet thickness corresponds therefore to a thickness of 4 to 5 grains. The grains are not randomly oriented but are assumed to show a [1 1 1] // ND fibres, resulting from recrystallization as suggests the literature on iron silicon steels [35,36]. The ideal texture for non-oriented silicon steel is (001) [uv0] where each grain has two <1 0 0> directions in the sheet plane, and the properties are nearly isotropic but no industrial process has been developed to obtain this ideal structure yet [37].

M330-35A is a soft and ductile material with a Young modulus E=186 GPa and an elongation to fracture A=28%.

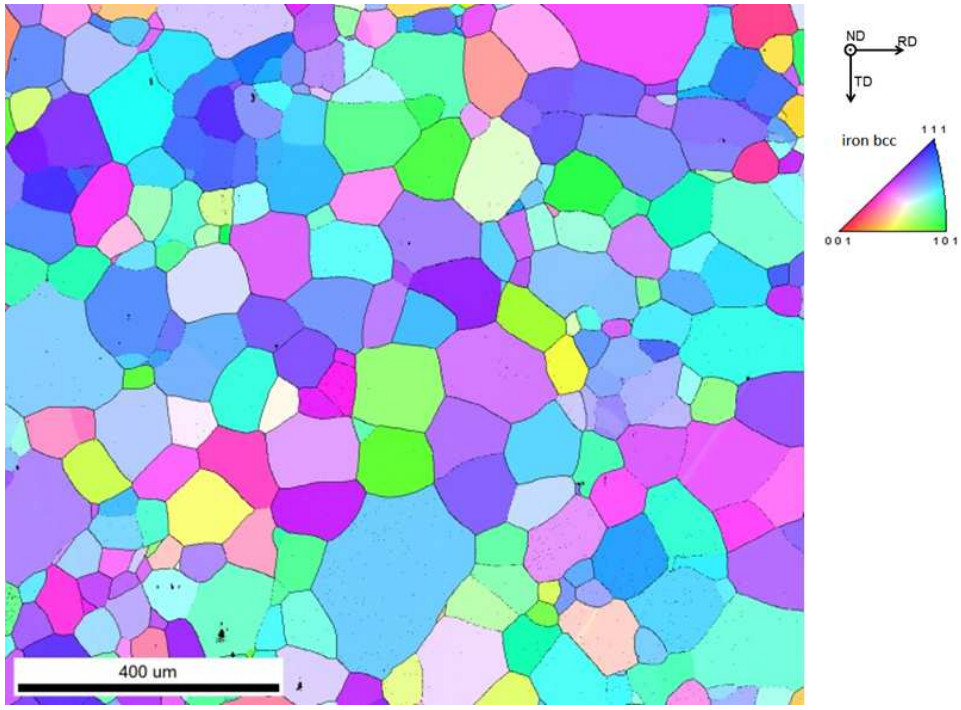

Figure 1: Microstructure of the M330-35A steel

2.2. Fatigue tests

In the previous studies, the main idea was to perform conventional Low Cycle Fatigue (LCF) tests on smooth specimen to understand the behaviour of the M330-35A steel. In the present case, the purpose is double. By making a notch in a flat sample, this reproduces a shape feature of a real component and ensure stress concentrators which may modify the local strain levels.

The LCF tests were carried out on a MTS servo-hydraulic machine on the same shape used in the previous investigations unlike the introduction of a rounded notch at the mid place of an edge of the gage length. With this specimen shape (cf. figure 2.a), it is not relevant to perform strain controlled LCF tests. Hence, a load control ranging from 0 to 700 N in a push-pull mode and with a triangular wave form was used instead.

2.3. Digital Image Correlation (DIC)

The DIC analysis, which consists in an advanced non-contact optical technique for displacement measurement, has been performed on a 2D system from GOM system (Gesellschaft für Optische Messtechnik). The considered system is constituted of a CCD camera, fitted with a 100mm lens, has a resolution of 2448*2050 pixels and a maximum frame rate of 15Hz. The post-processing of the data was performed with ARAMIS ® v6.3.0. software (GOM mbH, Braunschweig, Germany).

To conduct the DIC analyses, the notched specimen was first mechanically polished up to 3µm. Then, to obtain a speckle surface, a white antireflection paint was applied uniformly on the surface. Once it was dry, a graphite-based spray is applied in order to obtain correct grey distribution from the random repartition of black dots on the surface (Figure 2b). This preparation is crucial in order to have enough contrast and pattern features that allows to perform comparative analysis. [38,39]

The sample was then put into the fatigue testing machine and the camera was placed in front of the specimen at 90° to its surface (Figure 2c).

Image acquisition was performed before the fatigue test and during the cycle number N=1, 10, 11, 50, 100, 500, 1000 and 2000. The framerate acquisition, coupled with a strobe effect, allows to acquire around 30 snapshots per cycle.

Thanks to those patterns acquisition, the residual strain field in the unloading state has been evaluated by comparing the DIC data taken at the minimum stress at each fatigue cycles in comparison to the reference image taken before the fatigue test.

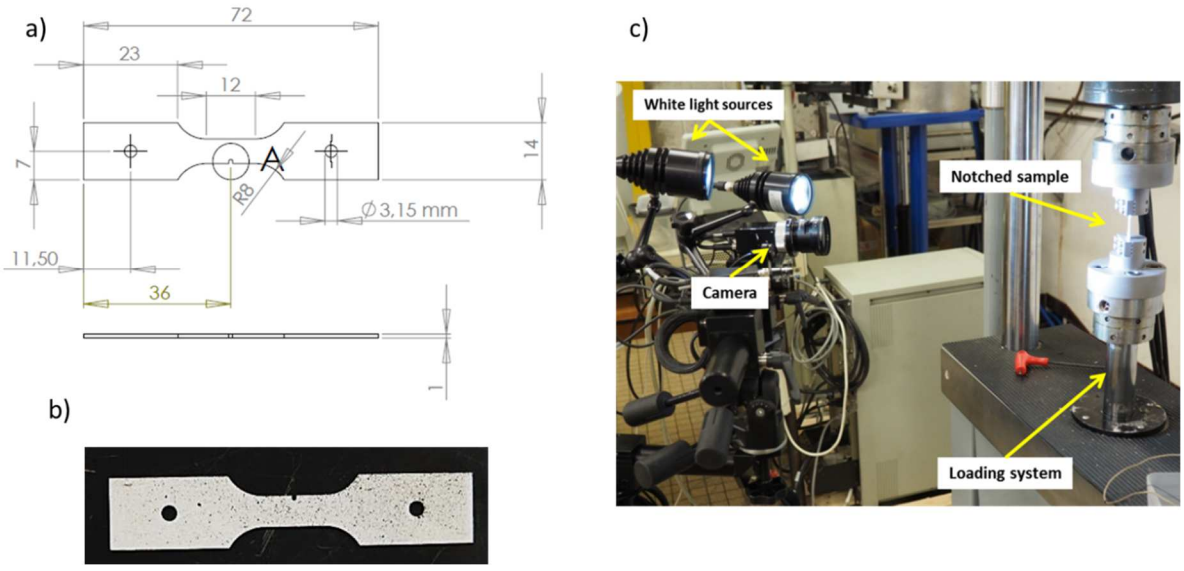

Figure 2: (a) Dimensions of the notched sample, (b) Speckle surface of a notched sample and (c) experimental set-up

2.4. Electron Back Scatter Diffraction

EBSD analysis have been carried out on a FEI Quanta 400 scanning electron microscope fitted with an Oxford Instruments EDS/EBSD system. The purpose was to obtain EBSD pattern which processing provides localisation of the strain at a mesoscopic scale.

A Nordlys CCD camera was used for pattern acquisition. Data were recorded at 1 µm step size using Oxford Instruments Aztec software. The analyses were carried out using both Oxford Instruments Channel 5 and TSL OIM 7 commercial software. By choosing the highest possible image resolution for pattern processing and by optimising the Hough transform parameters, an angular resolution of about 0.3° has been measured. As the grain size of the studied steel is relatively large, the considered step size for acquisition (1 µm), has been chosen according to the Chen *et al*. optimization method [40]. The observations were made on zones of 800 µm x 450 µm in the centre of the useful area of the fatigue samples.

The local strain levels of the Fe-3Si steel were considered through the Image Quality (IQ) of the pattern and the study of local misorientation. As kernel and grain based approaches have been fully investigated in a previous work [32], two criteria are considered here, respectively GROD and GOS as

148 they provide more evidences of the local strain. Those criteria, which belong to the grain-based
149 approach, are detailed hereafter.

150 Grain Reference Orientation Deviation (GROD) is based on the misorientation between a reference
151 point of that grain and the other points. The reference point can be the mean misorientation of the
152 grain or the point of the grain where the KAM is the lowest. Note that the KAM value is defined as
153 the mean value of misorientation a pixel and its neighbours providing that misorientation does not
154 exceed 5°, which should correspond to a Low Angle Grain Boundary (LAGB). It is defined by equation
155 (1-2).

$$GROD_i = \omega_{ik} \quad (1)$$

156 With ω_{ik} the deviation angle between orientation of pixel I and reference orientation of grain k.
157 This GROD criterion is sensitive to the orientation heterogeneities that evolve during deformation.

158 Grain Orientation Spread (GOS) is based on the misorientation averaged on the whole grain and is
159 defined by equation (5-4). In this mode each point in the grain is shaded with the same colour in the
160 maps.

$$GOS_k = \frac{1}{M}\sum_{i=1}^{M} GROD_i \quad (2)$$

161 With M the numbers of pixel within the grain k.

162 Here, the GOS criterion indicates the grains, as defined by orientation parameters, for which the
163 orientation heterogeneities are the most important.

164 3. Results and discussion

165 3.1. DIC displacement field measurements

166 As mention previously, the residual displacement field in the deformed image was estimated with
167 the Aramis software by comparison with the initial image of the non-deformed state. From this first
168 set of data, the strain along the Y axis (i.e. loading axis), ε_Y, and shear strain, ε_{XY} were then calculated

at each stage. The strain distributions at F_{max} are shown in Figure 3 as a function of the number of cycles. Strain was measured with an error of 0.1%.

These results highlight the longitudinal strain localisation at the notch root and the shear bands and the shear strain in the shear bands. Due to the subset size (9 pixels), which corresponds to a DIC spatial resolution of 210 µm, the strain distribution in the exact vicinity of the notch cannot be precisely evaluated.

The evolution of the longitudinal strain ε_Y at the point where the strain is the maximum at the notch root was also evaluated and reported in Figure 4a and 4b.

Figure 4a shows that the cyclic evolution of the longitudinal strain is in agreement with the cyclic load, the strain increases when the force increases. Moreover, the maximum strain increases with the number of cycles up to N=500 cycles. From this number of cycles, the strain evolution is in a stabilised regime where no more plastic straining occurs as shown in the hysteresis curves (figure 4b).

Note that the presence of a notch induces strain localisation and a behaviour different from the one observed on smooth samples. Indeed, on a smooth specimen, until the propagation of the main crack, the strain partition is more or less homogeneous. The resulting measurement by DIC would be similar to the one obtained with a classical extensometer. In the current case, the most relevant comparison with smooth samples is to consider an incremental step test method, which is generally used to obtain a cyclic stress-strain curve. This test was performed under load control mode and the strain was measured by an extensometer. Once the strain was stabilised, the step was finished and the load was increased for the following loading step. The advantage of this test is that it needs only one sample. However, it is important to specify a parameter for the end of a step which is characterised by a stabilisation of the deformation during cycling. It is considered that the stabilisation is reached when the difference between two cycles is inferior or equal to 10^{-4}/cycle as it is shown in Figure 5a.

194 Table 1 summaries the results for the considered Fe-3Si steel. The obtained cyclic stress-strain curve
195 is represented in Figure 5b and compared with the monotonic tensile curve. A cyclic hardening is
196 observed and for a same stress, the strain is more important in monotonic loading than in cyclic
197 loading.

198 Hence, the value of 3% measured by DIC at the notch root after 2000 cycles results from the cycling
199 at a positive mean stress. When a material is subjected to such condition of loading, it is observed
200 that the hysteresis loops progressively shift toward positive value of strain and a steady state can be
201 observed or not. The latter case refers to the ratcheting effect and the total deformation
202 continuously increases [41]. When a steady state is observed, the total strain remains constant and
203 the stress-strain evolution evolve either in an elastic way or with plasticity. Figure 4b suggests that a
204 steady state has occurred, the loops do not shift anymore with increasing number of cycles since 500
205 cycles and very small plastic strain can be measured on the hysteresis loops. Therefore, the strain
206 value of 3 % results from an accumulation of cycles. Nevertheless, one may not exclude that the
207 strain at the notch tip resulting from each type of loading would be different from an equivalent
208 static loading. Indeed, the strain assessed by the DIC technique is only based on the processing of
209 displacement field. However, the microstructure behind will be different since the plasticity at the
210 notch root would activate differently the dislocation displacement.

211 Note that ratcheting effect also occurs during the incremental step test method. Moreover, the
212 behaviour of the steel in the localised deformation areas (as observed visually on Figure 4a)
213 corresponds to zones for which the material response is similar to regimes $\sigma_{ys} < \sigma_{max} < 1.2\ \sigma_{ys}$.
214 Nevertheless, due to stress concentration effect, the associated strain amplitude is more
215 pronounced.

216 Then, in order to correlate these results in a more precise way, both EBSD and ECCI techniques are
217 necessary to be used to complete the DIC measurements otherwise incorrect plasticity mechanisms
218 may be proposed.

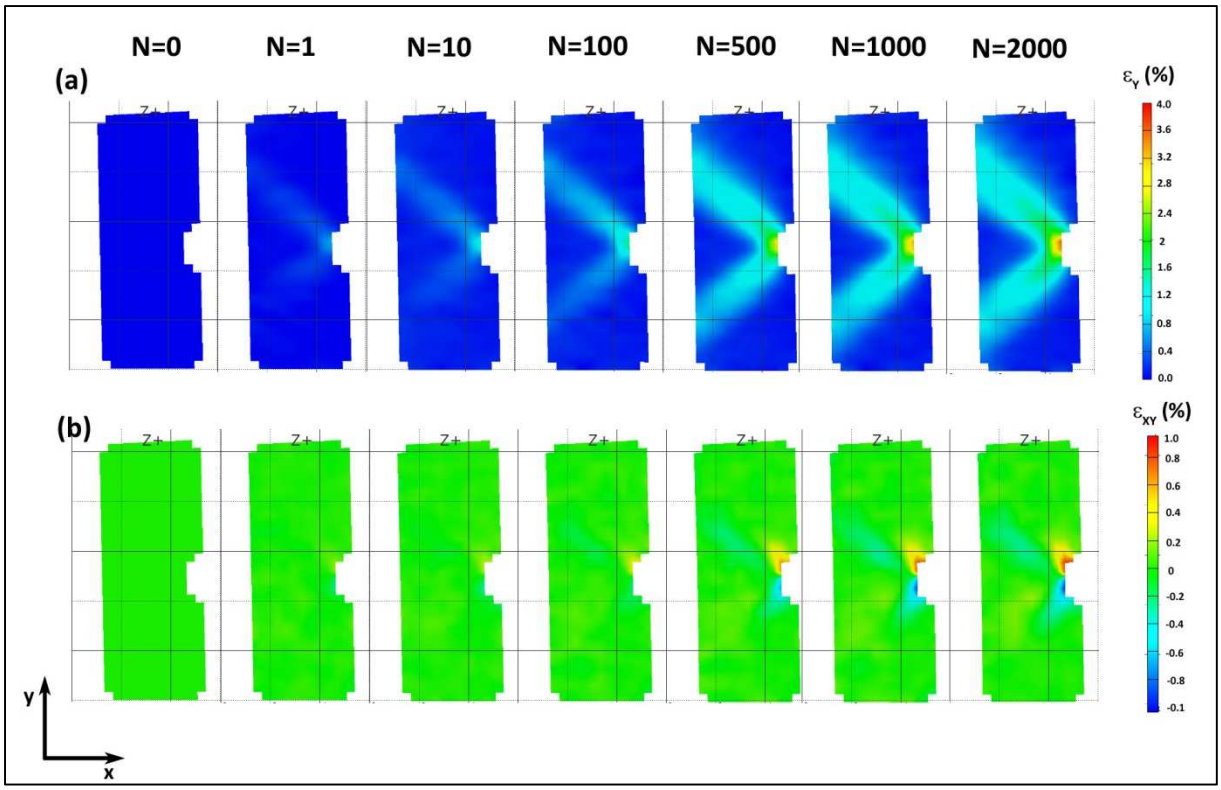

Figure 3: (a) Longitudinal strain, ε_Y, and (b) shear strain, ε_{XY}, distribution estimation by DIC of a notched sample subjected to cyclic loading at Fmax for cycle number N=0, 1, 10, 100, 500, 1000 and 2000

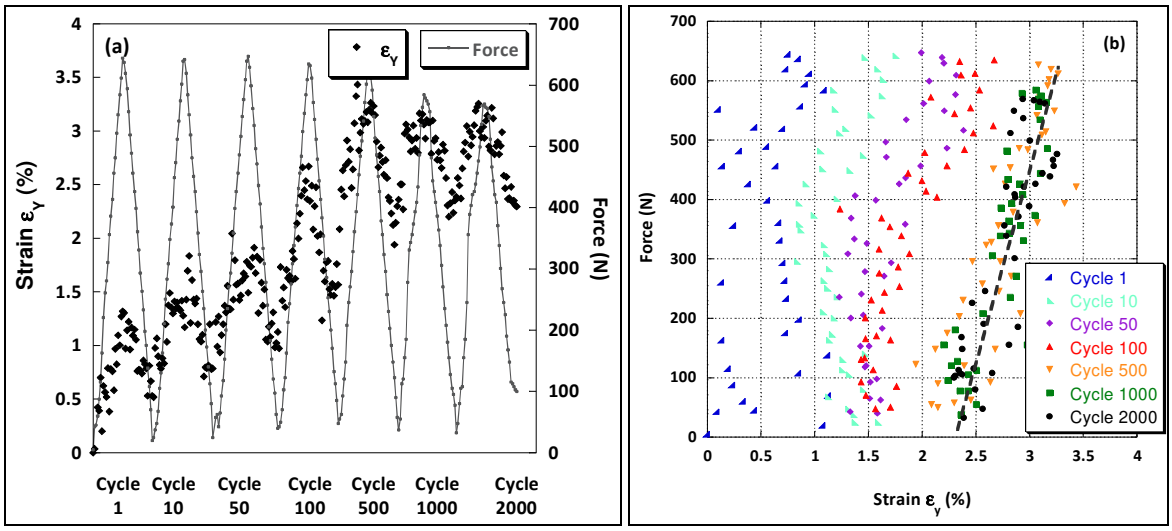

Figure 4: (a) Evolution of the longitudinal strain ε_Y at the notch root and (b) hysteresis curves as a function of the cycle number

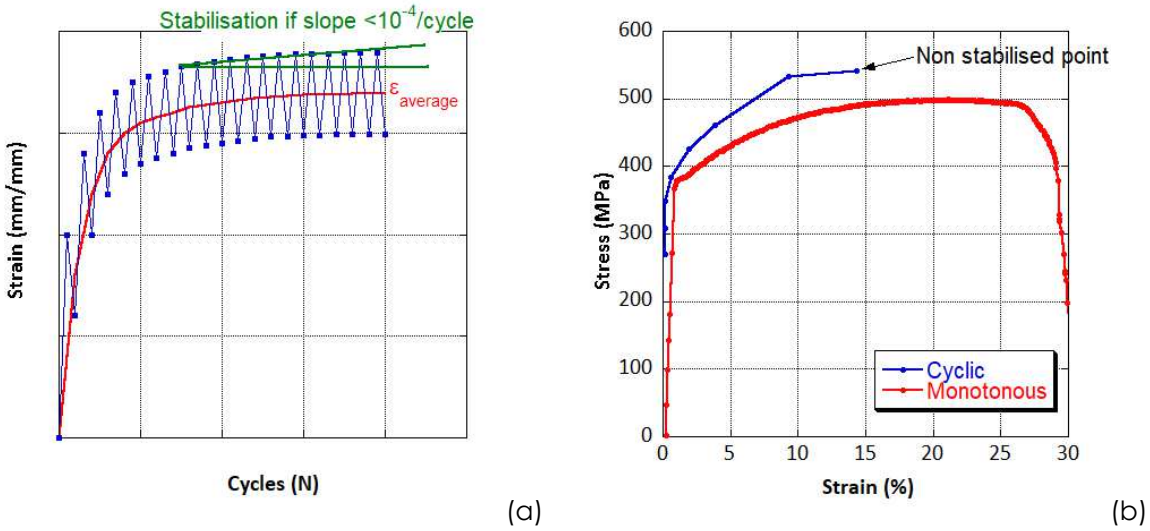

Figure 5: (a) Stabilisation criteria of a step (b) Cyclic vs monotonic stress-strain curve of the Fe-3Si steel

Table 1: Summary of the fatigue test by steps

σ_{max}	Material response			Strain (stabilised regime)			Number of cycles to reach the stabilisation criteria
	σ_{max} (MPa)	σ_{min} (MPa)	σ_a (MPa)	ε_{max} (%)	ε_{min} (%)	$\Delta\varepsilon_t$ (%)	
0.7 σ_{ys}	253	4.4	129.02	0.126	0.008	0.118	100
0.8 σ_{ys}	292	3.6	148	0.146	0.008	0.138	100
0.9 σ_{ys}	330	2	166.42	0.175	0.018	0.158	200
σ_{ys}	364	3.2	138.62	0.622	0.46	0.162	4000
1.1 σ_{ys}	403	1.2	202.22	1.89	1.69	0.2	4000
1.2 σ_{ys}	437	4.8	221.03	3.83	3.59	0.24	5000
1.3 σ_{ys}	495	29.6	262.4	9.31	9.02	0.29	500
1.4 σ_{ys}	508	7.2	257.83	15	14.7	0.34	Non stabilised

3.2. EBSD analysis

To highlight the ability of the EBSD tool to indicate the strain localisation effect, EBSD analyses were carried out on the notched sample used for the study of strain distribution by DIC, at N=2000 cycles. Figure 6 indicates the areas considered for the EBSD analysis on the normal strain distribution map measured by DIC. The two considered zones are, for the first one, just behind the notch (zone 1) and in the vicinity of a shear band (zone 2).

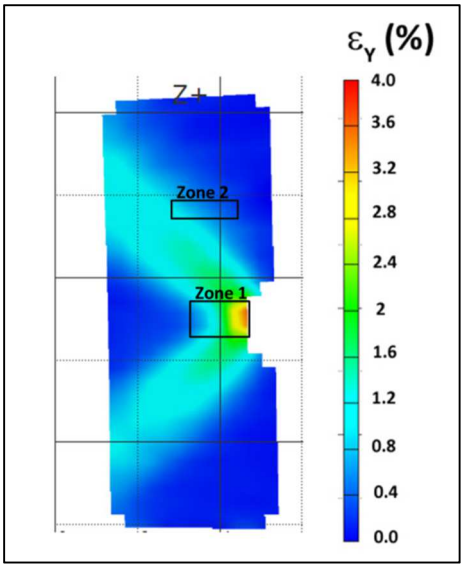

Figure 6: Localisation of complementary EBSD analyses

In order to have an overview of these broad areas, several maps of 800x450µm were recorded and stitched to each other in order to form a global map of 1570 x 750 µm² (279 grains) for zone 1 and of 3000 * 815 µm² (483 grains) for zone 2. The corresponding colour coded IPF, GROD and GOS maps of zone 1 and zone 2 are shown in Figure 7 and Figure 8 respectively.

Both IPF, GROD and GOS maps of the zone 1 (figure 7) show orientation heterogeneities close to the notch. For the IPF map (figure 7a), these heterogeneities correspond to local variation of the colour contrast. The GROD map (figure 7b) shows that close to the notch (on the right) warmer colours are obtained, which is the sign of higher misorientation (up to 8°) and strong localisation of orientation

heterogeneities at the grain boundaries. Further away from the notch, grain interiors become almost free from misorientation gradients while those latter remain localised at the grain boundaries vicinity.

The GOS map (figure 7c) attributes a grain colour that depends on the presence of misorientation gradients within the grain. A gradient colour mapping is introduced: as the misorientation gradients inside the grain become stronger, the colour evaluates from cold (blue, 0°) to warm (red, 5°) colours.

The EBSD investigation of the zone 1 shows that the grains become less misoriented away from the notch. This observation is consistent with the strain localisation in this area. Indeed, strain is correlated with the presence of both statistically stored dislocations (SSD) and geometrically necessary dislocations (GND), and grain misorientation in deformed areas are inherited from their presence. Moreover, the misorientation gradients observed inside the grain are consequences of different dislocations signatures in the grain interior (vein structures) and at the grain boundary (wall structures) [42].

For further examinations and correlation with microstructure details and measured DIC values, the global GOS map was divided in 4 subsets, defined with the black dot square areas of GOS map (figure 7c). The mean GOS, calculated in these subsets, are the following: $GOS_{mean,1}$=1.55, $GOSmean_{,2}$=0.89, $GOSmean_{,3}$=0.69, $GOSmean_{,4}$=0.6.

Regarding the zone 2, on the left of the map (figure 8b), there is a slight misorientation gradient within the grains, associated with a localisation at the grain boundary vicinity. Note that, some grains exhibit higher misorientations levels. The trend is different on the right side of the map, for which almost all the grains exhibit no misorientation gradient. This observation is confirmed by the GOS map (figure 8c), which show a higher amount of grain free from misorientation gradient on the on the right of the map. This observation is coherent with the DIC map (figure 6). Indeed, the presence of the shear band which induces higher strain in the left part of the zone 2.

In this zone, the mean GOS (calculated from the black dot square area of the GOS map in figure 8) is 0.62 and corresponds to the value $GOS_{mean,4}$ measured previously.

This quick comparison between, *i.* the DIC strain map of the notch sample at N=2000 cycles and *ii.* the localisation of the areas on which EBSD analysis has been carried out, confirms the ability of EBSD to emphasize the plastic strain localisation.

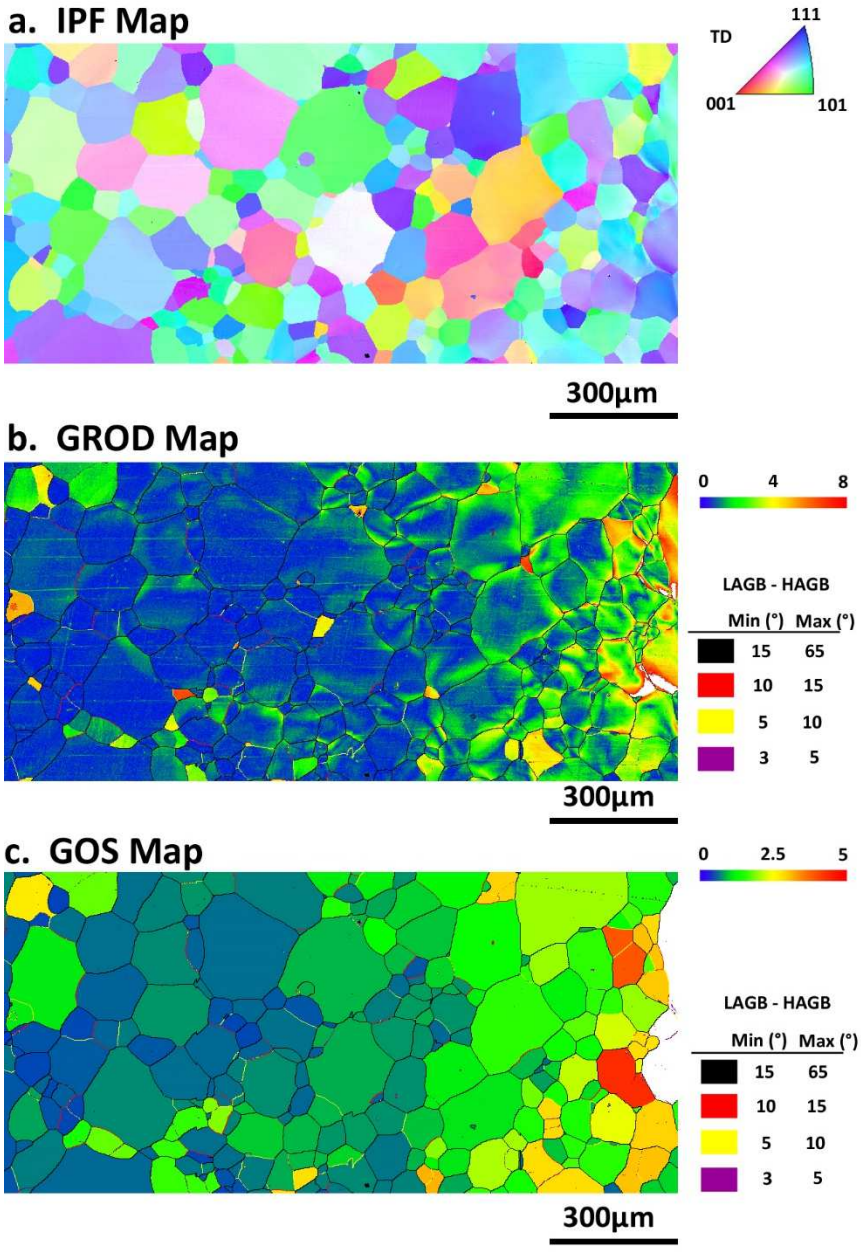

Figure 7: (a) IPF in TD direction, (b) GROD and (c) GOS maps of the Zone 1 of the sample (notch on the right)

283

284

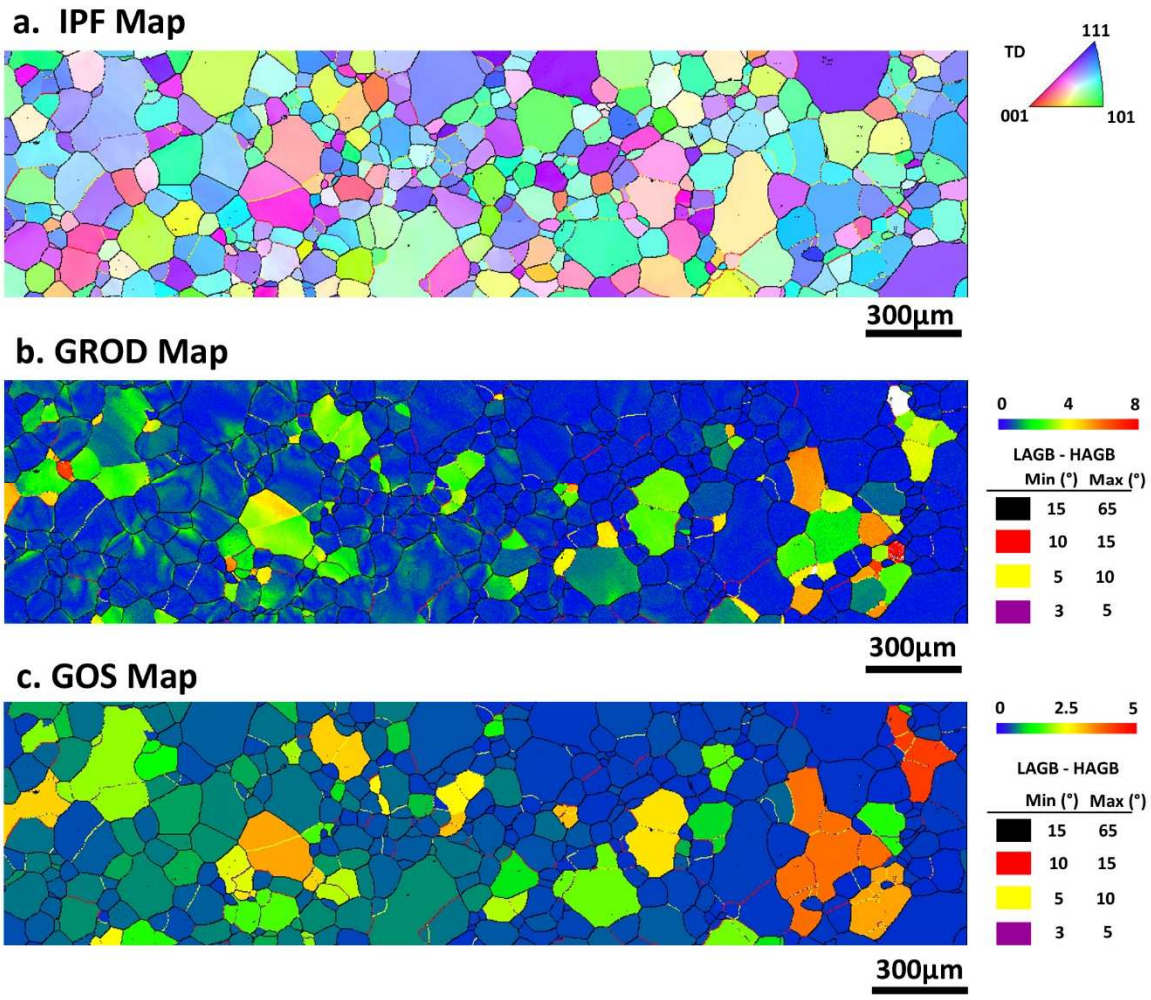

285

286 **Figure 8: IPF in TD direction, GROD and GOS maps of the Zone 2 of the sample**

287

288

3.3. Deeper assessment of the cyclic plastic strain coupling EBSD, ECCI and DIC data

As mentioned previously, the EBSD maps and corresponding measurements give a clear indication of the strain localisation in the deformed notched sample. The LCF behaviour of the non-notched samples has been fully investigated in previous works [32–34] and the obtained results are used to correlate the strain levels measured with DIC and misorientations measured with EBSD for the notched sample to an equivalent total strain variation of non – notched samples.

The main issues from these previous investigations are summarized in figure 9. As the total applied strain increases, the Fe-3% Si steel exhibits behaviours equivalent to low temperature and to high temperature regimes. For the lowest strain amplitudes, dislocation sources are activated within the grain and dislocation slip is planar, as also reported for short range ordered alloys. While restricted by high friction related to the Fe-Si clusters, the dislocation glide length remains sufficient to accommodate the required strain in a quasi-static regime. This leads to transgranular cracking. By contrast, for the highest level of deformation, plastic strains and cumulated strains can successfully reduce the restricted effect of the Fe-Si short range order on the plasticity. Grains accommodate individually plastic deformation, but dislocation glide through grains is difficult. The resulting incompatibility effects produce intergranular stresses and strain localisation that generate intergranular crack initiation (Figure 9a).

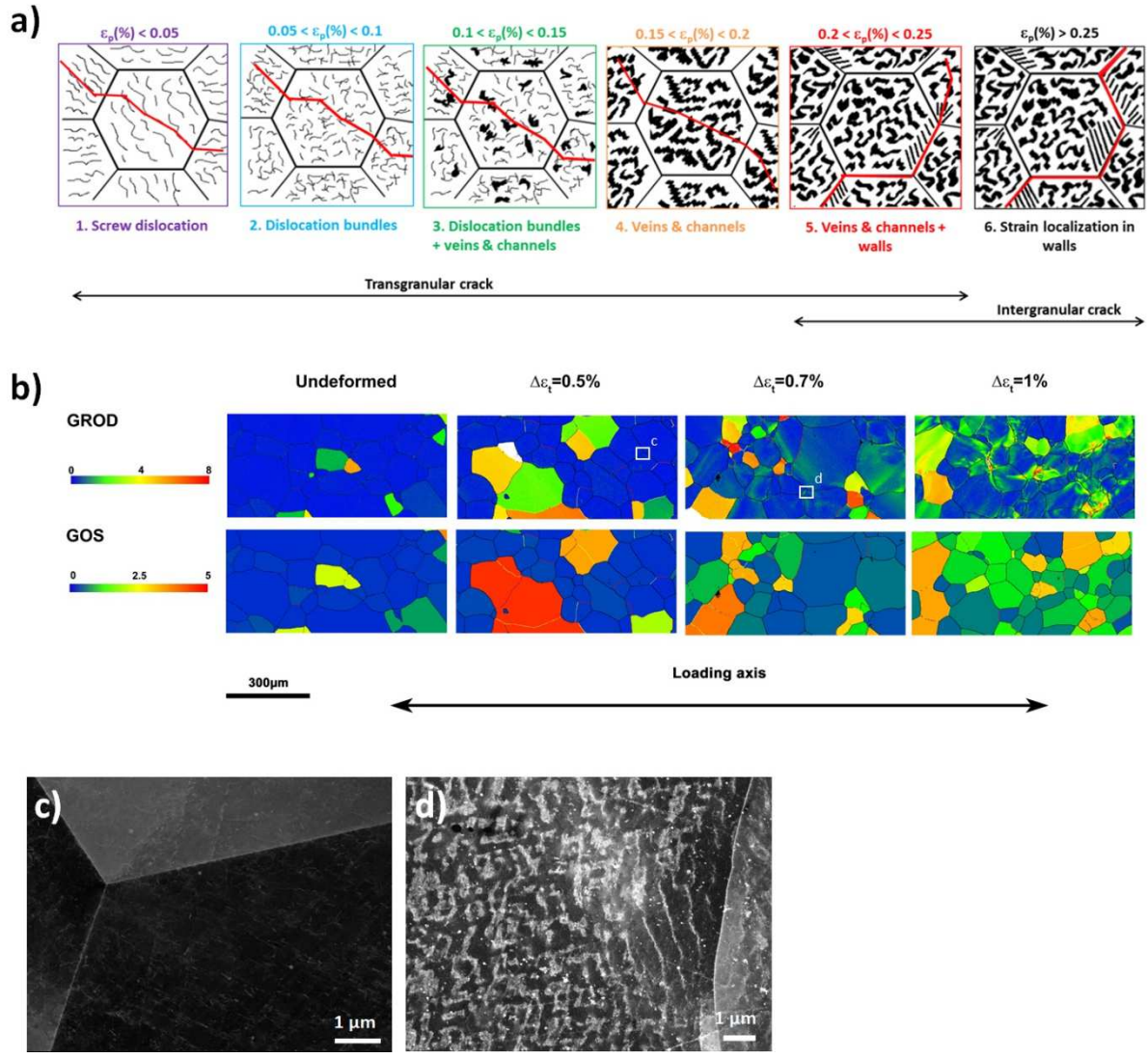

306

307 **Figure 9: (a) Schematic representation of dislocations structures involved in the damage of the Fe-Si steel (b) Evolution of**
308 **the GROD and GOS maps for LCF test on smooth specimens as a function of the applied strain (c) and (d) corresponding**
309 **ECCI observations**

310

311 This strain accommodation was suggested from EBSD data processing and imaged by ECCI and two
312 major conclusions were highlighted (Figure 9b, 9c and 9d). Firstly, the strain accommodation with the
313 grains is associated by the formation of dislocation structures commonly described in fatigue [43–
314 45]. Nevertheless, due to the stress incompatibility at the grain boundary, the corresponding strain
315 localisation results in variation of dislocations structure between the grain interiors (vein and
316 channels) and the vicinity of the grain boundary (walls). This difference can be clearly evaluated in

terms of misorientations, since veins consists of an agglomeration of edge dipoles, surrounded by GNDs. By contrast, channels only exhibit very few SSDs. In addition, walls are veins evolutions for which edge dipoles accumulate and then confine while misorientation increases [42,46–48]. Here both step size and angular resolution, considered in the present analysis, do not permit a fine distinction between dislocations rich veins/walls zones and channels. Nevertheless the transition between veins/channels and walls results in gradients that were clearly observed through the GROD criterion [32,49].

On the second hand, a clear correlation between the appearance of a strain localisation as a function of the applied strain level has been evaluated by taking into account the GOS criterion. Indeed, such a strain localisation is correlated to misorientation gradients at the grain interfaces. The deeper the walls structures spread inside the grains, the higher become the gradient. In addition, the number of grains for which such a localisation effect occur also increases with higher total strain levels.

From these observations, there is a way to estimate the equivalent strain undergone by the material in the different areas of zone 1 based on the relation established in figure 10 (a) in which the mean GOS value is correlated to the total strain variation. A numerical correlation is done for an estimation of the GOS value corresponding to $\Delta\varepsilon_t > 1.0\%$.

Therefore, the mean GOS values previously measured on the notched specimen in zone 1 are reported in Figure 10 (a) and the equivalent total strain variations are deduced by graphical reading. In addition, these mean GOS values are plotted against the normal local strain value obtained by DIC in Figure 10 (b).

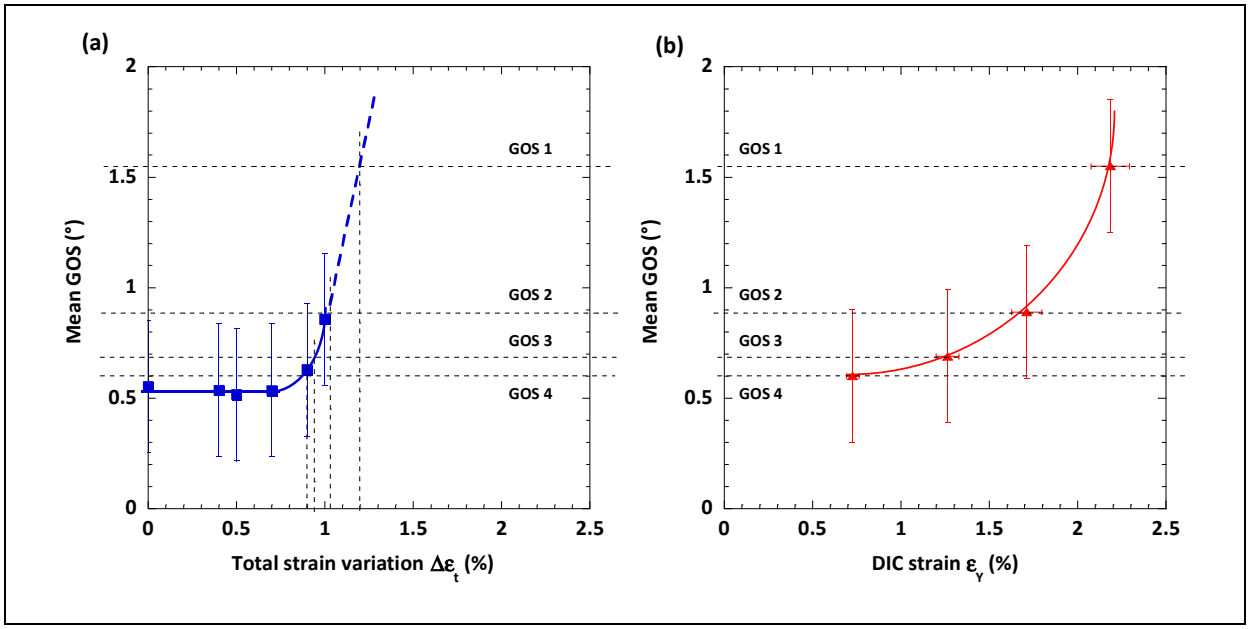

Figure 10: (a) Equivalent total strain estimation in the different zones of the notched specimen from the relation between GOS and total strain variation established on smooth specimen and (b) mean GOS value of the different zones of the notched specimen versus the normal strain measured by DIC

It can be noticed here that a direct correspondence of the normal strain calculated by DIC on the notched sample with the total strain variation of the smooth samples is difficult and more especially for the highest strains. Indeed, the LCF study on smooth samples was performed only up to $\Delta\varepsilon_t$=1%. Above this strain range, the dislocation structure and mean GOS value in the case of smooth sample are unknown. Also, a precise estimation of the strain by the GOS criteria over a small area is difficult because large grain size hinders statistical analyses and strain measurements by DIC are made on a macroscopic scale.

The observation of the dislocation structure in area 1 of zone 1 (zone where highest strains are reached) by ECCI is shown in Figure 11. It reveals irregular dislocation walls in the process of transforming into dislocation cells.

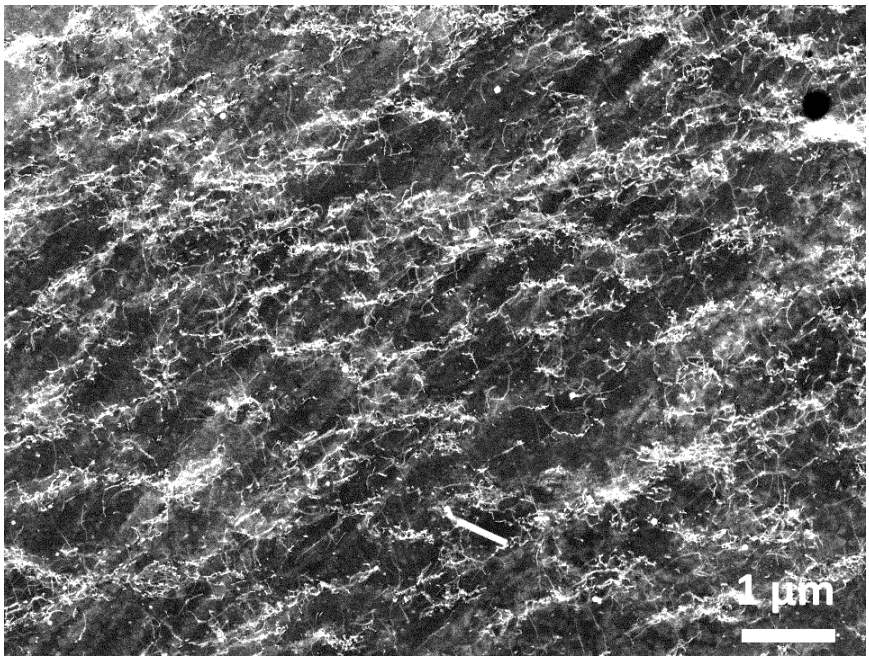

Figure 11: ECCI micrograph of the dislocation structure near the notch

This structure expresses a more advanced deformation state than those observed in smooth samples loaded at $\Delta\varepsilon_t$=1%. Therefore, this is consistent with the fact that in area 1, strains superior to the equivalent total strain variation of 1% are reached and that a ratcheting effect, leading to mean strain of 3% is observed.

Furthermore, referring to these new results, one possible evolution of mean GOS as a function of total strain variation is shown in Figure 12. In this figure, the GOS evolution with the total strain variation is depicted in three stages. During the first stage, the mean GOS is constant over a wide strain range (from $\Delta\varepsilon_t$=0% to $\Delta\varepsilon_t$=0.7%) because the dislocation structure is homogeneous in the grain. During the second stage, the mean GOS increases rapidly with the total strain variation (from $\Delta\varepsilon_t$=0.7% to $\Delta\varepsilon_t$=1%), this is due to localisation of the strain at grain boundary and higher misorientation in this zone.

The linear increase of the mean GOS with $\Delta\varepsilon_t$ reflects the increasing ratio between dipolar walls in the vicinity of grain boundaries and veins in the grain interiors. When the grain is completely filled out with walls, an increase in strain should trigger the transformation of walls into cells. A new regime, the third stage, takes then place.

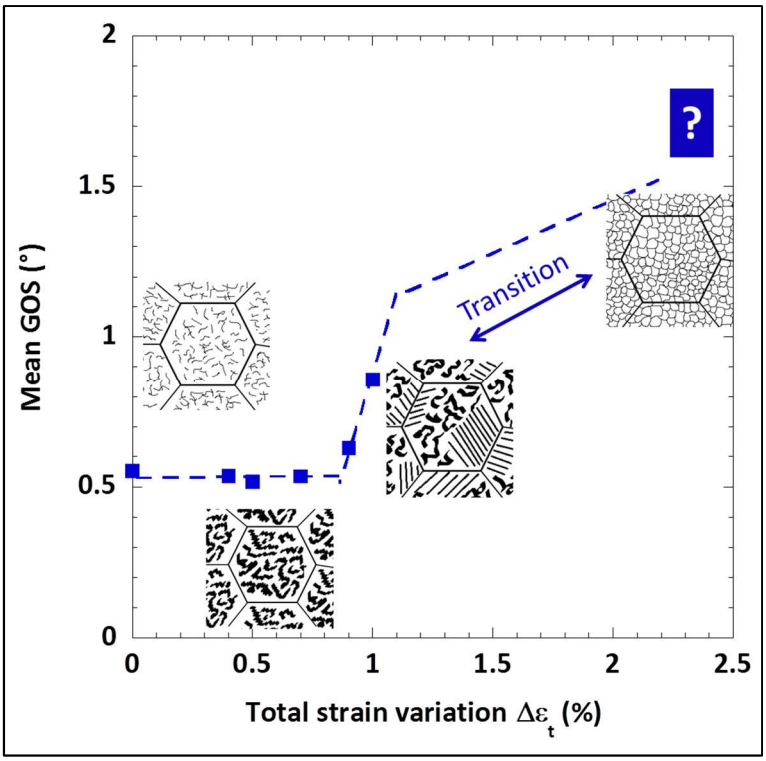

369

370 **Figure 12: Evolution of mean GOS with total strain variation**

371

372 The proposed approach, based on a comparison between GROD/GOS misorientation criteria and
373 linked with DIC measurements and ECCI imaging, differs from the current approaches developed
374 around EBSD, ECCI and DIC. Although the selected EBSD acquisition parameters (step size, EBSP
375 resolution) do not permit to detail locally the Nye tensor and calculate precisely the dislocations
376 densities by lacking of both high spatial resolution and high angular resolution, it allows the
377 comparison of different zones in the sample and propose a clear view of the local plasticity levels.

378 Indeed, the major trends of the new EBSD developments are based on high resolution EBSD (HR-
379 EBSD) or Cross-Correlation EBSD (CC-EBSD). Nevertheless, most of the works do not face directly the
380 calculated GNDs densities, distributions and stress/strain fields with corresponding dislocations
381 structures for FCC structures (single phase copper and nickel alloys) [30,50,51]. A more recent
382 approach makes a comparison between cECCI and CC-EBSD in order to explain how entangled
383 dislocations evolve to wall and channels structure in a DP steel [52]. However, in that latter case, a

384 huge amount of data, coupled with a fine step size in terms of EBSD acquisition are required.
385 Although the corresponding results are highly valuable and bring microscopic details on how the
386 microstructure evolve during cycling, the scale limitation remains restraint when taking into account
387 a large zone with a possible variation in terms of dislocations structuration as observed in the
388 present study.

389 The same kind of observation can be done for DIC measurements, as for cyclic plasticity, the
390 measurements are mainly related to the residual strains or the maximum strains, depending on how
391 and when the data are acquired.

392

393 **Conclusions**

394 The current work aimed at proposing a judicious combination of microscopy related measurements
395 and observations to understand in both qualitative and quantitative ways the effect of cyclic loading
396 on the microstructure response of a Fe-3%Si steel. Three complementary techniques have been
397 considered: EBSD, ECCI and DIC.

398 Although each of the techniques is well known and its application to plastic strain determination well
399 documented in the literature, some considerations have to be taken into account.

400 • EBSD analysis, conducting with right selected parameters, can lead to a clear overview of the
401 plastic strain. However, a particular attention has to be done when post-processing the data.
402 In general, EBSD data are only linked to misorientation and pattern quality measurements.
403 The first aspect indirectly characterises the GND dislocations, while the second may be
404 related with both GND and SSD dislocations. The corresponding strain and stress field can
405 also derivate from the misorientation measurements, but the acquisition step-size is of prime
406 importance.

- ECCI gives a clear observation of the dislocations, as these latter would be observed by TEM. However, this technique cannot make a distinction between SSDs and GNDs.
- Strain fields obtained through DIC measurements are easily understood. When characterising the strain fields coming from a cyclic loading, the situation appears to be a bit more complex.

The combination of the data coming from the three different techniques avoid to make some mistakes. The misorientation criteria obtained with EBSD can easily been associated to dislocations structuration, as comparing with ECCI observations. In a same manner, such measurements can also be related to strain levels determined by DIC.

Applied on a notched specimen made of Fe-3%Si steel, submitted to cyclic loading, new details on the materials behaviour have been obtained.

The DIC measurements clearly emphasise the strain localisation effect during cycling. In addition, it points out a ratcheting effect, which is more pronounced close to the notch. However, taking into account the resulting deformation measurement from the DIC data alone does not reflect the accumulated plasticity of the material. Hence, the use of abacuses, linking local misorientation and total strain variation, on one hand and misorientation and the DIC measurements of residual cyclic strain on the other hand, confirms a higher accumulated cyclic strain in the notch region, which can be related to the combination of a higher strain amplitude with a higher mean strain. This has also been confirmed by the ECCI observations that show irregular dislocation walls in the process of transforming into dislocation cells.

Acknowledgment

The authors thank Valeo France for Financial support, Mr. Golek and Mr. Creton for the technical help. The SEM facility in Lille (France) is supported by the Conseil Régional du Nord-Pas de Calais, and the European Regional Development Fund (ERDF).

Data availability statement

The raw/processed data required to reproduce these findings cannot be shared at this time due to legal or ethical reasons

438 **References**

439 [1] W. Zhang, Y. Zhang, H. Li, X. Gu, Experimental investigation of fatigue bond behavior between
440 deformed steel bar and concrete, Cem. Concr. Compos. 108 (2020) 103515.
441 doi:10.1016/j.cemconcomp.2020.103515.

442 [2] M. Tripathi, R.P. Dhakal, F. Dashti, L.M. Massone, Low-cycle fatigue behaviour of reinforcing
443 bars including the effect of inelastic buckling, Constr. Build. Mater. 190 (2018) 1226–1235.
444 doi:10.1016/j.conbuildmat.2018.09.192.

445 [3] J.-B. Vogt, C. Carle, J. Bouquerel, I. Proriol Serre, Behaviour of short and long cracks in air and
446 in liquid metal in T91 steel, in: MATEC Web Conf., 2018.
447 doi:10.1051/matecconf/201816503016.

448 [4] J.B. Vogt, S. Argillier, J.P. Massoud, V. Prunier, Fatigue damage evaluation of a power plant
449 component from analysis of the dislocation structures, Eng. Fail. Anal. 7 (2000) 301–310.
450 doi:10.1016/S1350-6307(99)00034-5.

451 [5] M. Shirani, G. Härkegård, A review on fatigue design of heavy section EN-GJS-400-18-LT
452 ductile iron wind turbine castings, Energy Equip. Syst. 2 (2014) 5–24.
453 doi:10.22059/ees.2014.5008.

454 [6] R. Branco, J.D. Costa, F. Berto, A. Kotousov, F. V. Antunes, Fatigue crack initiation behaviour of
455 notched 34CrNiMo6 steel bars under proportional bending-torsion loading, Int. J. Fatigue.
456 (2020). doi:10.1016/j.ijfatigue.2019.105268.

457 [7] F.M. Firouz, E. Mohamed, A. Lotfy, A. Daoud, M.T. Abou El-Khair, Thermal expansion and
458 fatigue properties of automotive brake rotor made of AlSi–SiC composites, Mater. Res.
459 Express. 6 (2020) 1265d2. doi:10.1088/2053-1591/ab6129.

460 [8] M. Fonte, P. Duarte, V. Anes, M. Freitas, L. Reis, On the assessment of fatigue life of marine
461 diesel engine crankshafts, Eng. Fail. Anal. 56 (2015) 51–57.

462 doi:10.1016/j.engfailanal.2015.04.014.

463 [9] Z. Zheng, S. Yuan, T. Sun, S. Pan, Fractographic study of fatigue cracks in a steel car wheel,
464 Eng. Fail. Anal. 47 (2015) 199–207. doi:10.1016/j.engfailanal.2014.09.010.

465 [10] S.M.O. Tavares, P.M.S.T. de Castro, An overview of fatigue in aircraft structures, Fatigue Fract.
466 Eng. Mater. Struct. 40 (2017) 1510–1529. doi:10.1111/ffe.12631.

467 [11] L. Li, A. Kedous-Lebouc, A. Foggia, J.C. Mipo, Influence of magnetic materials on claw pole
468 machines behavior, IEEE Trans. Magn. 46 (2010) 574–577. doi:10.1109/TMAG.2009.2032520.

469 [12] G. Cai, C. Li, B. Cai, Q. Wang, An investigation on the role of texture evolution and ordered
470 phase transition in soft magnetic properties of Fe–6.5 wt%Si electrical steel, J. Magn. Magn.
471 Mater. 430 (2017) 70–77. doi:10.1016/j.jmmm.2017.01.054.

472 [13] M. Reinlein, T. Hubert, A. Hoffmann, A. Kremser, Optimization of analytical iron loss
473 approaches for electrical machines, 2013 3rd Int. Electr. Drives Prod. Conf. EDPC 2013 - Proc.
474 (2013) 1–7. doi:10.1109/EDPC.2013.6689759.

475 [14] F. Henrotte, S. Steentjes, K. Hameyer, C. Geuzaine, Iron loss calculation in steel laminations at
476 high frequencies, IEEE Trans. Magn. 50 (2014) 0–3. doi:10.1109/TMAG.2013.2282830.

477 [15] M. Sugiyama, M. Shibata, Application of Scanning Electron Microscope to Dislocation Imaging
478 in Steel, JEOL News. 46 (2011) 11–16. http://www.jeol.co.jp/en/applications/detail/780.html.

479 [16] S. Zaefferer, N.-N. Elhami, Theory and application of electron channelling contrast imaging
480 under controlled diffraction conditions, Acta Mater. 75 (2014) 20–50.
481 doi:10.1016/j.actamat.2014.04.018.

482 [17] J. Jiang, T.B. Britton, A.J. Wilkinson, Evolution of dislocation density distributions in copper
483 during tensile deformation, Acta Mater. 61 (2013) 7227–7239.
484 doi:10.1016/j.actamat.2013.08.027.

[18] J. Jiang, T.B. Britton, A.J. Wilkinson, Measurement of geometrically necessary dislocation density with high resolution electron backscatter diffraction: Effects of detector binning and step size, Ultramicroscopy. 125 (2013) 1–9. doi:10.1016/j.ultramic.2012.11.003.

[19] M. Hayakawa, M. Wakita, E. Nakayama, Damage evaluation of ferrite and ferrite-pearlite steel during fatigue crack initiation by EBSD, Adv. Mater. Res. 891–892 (2014) 410–415. doi:10.4028/www.scientific.net/AMR.891-892.410.

[20] M.J. Holzweissig, P. Kanagarajah, H.J. Maier, Digital image correlation at high temperatures for fatigue and phase transformation studies, J. Strain Anal. Eng. Des. 49 (2014) 204–211. doi:10.1177/0309324713498737.

[21] A.D. Darbal, M. Gemmi, J. Portillo, E. Rauch, S. Nicolopoulos, Nanoscale Automated Phase and Orientation Mapping in the TEM, Micros. Today. 20 (2012) 38–42. doi:10.1017/S1551929512000818.

[22] C. Rehrl, S. Kleber, T. Antretter, R. Pippan, A methodology to study crystal plasticity inside a compression test sample based on image correlation and EBSD, Mater. Charact. 62 (2011) 793–800. doi:10.1016/j.matchar.2011.05.009.

[23] G. L'hôte, C. Lafond, P. Steyer, S. Deschanel, T. Douillard, C. Langlois, S. Cazottes, Rotational-Electron Channeling Contrast Imaging analysis of dislocation structure in fatigued copper single crystal, Scr. Mater. 162 (2019) 103–107. doi:10.1016/j.scriptamat.2018.10.050.

[24] M.T. Welsch, M. Henning, M. Marx, H. Vehoff, Measuring the plastic zone size by Orientation Gradient Mapping (OGM) and Electron Channeling Contrast Imaging (ECCI), Adv. Eng. Mater. 9 (2007) 31–37. doi:10.1002/adem.200600195.

[25] T. Niendorf, J. Dadda, D. Canadinc, H.J. Maier, I. Karaman, Monitoring the fatigue-induced damage evolution in ultrafine-grained interstitial-free steel utilizing digital image correlation, Mater. Sci. Eng. A. 517 (2009) 225–234. doi:10.1016/j.msea.2009.04.053.

[26] A. Guery, F. Hild, F. Latourte, S. Roux, Slip activities in polycrystals determined by coupling DIC measurements with crystal plasticity calculations, Int. J. Plast. 81 (2016) 249–266. doi:10.1016/j.ijplas.2016.01.008.

[27] W. Abuzaid, H. Sehitoglu, J. Lambros, Plastic strain localization and fatigue micro-crack formation in Hastelloy X, Mater. Sci. Eng. A. 561 (2013) 507–519. doi:10.1016/j.msea.2012.10.072.

[28] E. Salvati, S. O'Connor, T. Sui, D. Nowell, A.M. Korsunsky, A study of overload effect on fatigue crack propagation using EBSD, FIB–DIC and FEM methods, Eng. Fract. Mech. 167 (2016) 210–223. doi:10.1016/j.engfracmech.2016.04.034.

[29] J. Nellessen, S. Sandlöbes, D. Raabe, Effects of strain amplitude, cycle number and orientation on low cycle fatigue microstructures in austenitic stainless steel studied by electron channelling contrast imaging, Acta Mater. 87 (2015) 86–99. doi:10.1016/j.actamat.2014.12.024.

[30] T. Zhang, J. Jiang, B. Britton, B. Shollock, F. Dunne, Crack nucleation using combined crystal plasticity modelling, high-resolution digital image correlation and high-resolution electron backscatter diffraction in a superalloy containing non-metallic inclusions under fatigue, Proc. R. Soc. A Math. Phys. Eng. Sci. 472 (2016). doi:10.1098/rspa.2015.0792.

[31] F. Bridier, J.C. Stinville, N. Vanderesse, P. Villechaise, P. Bocher, Microscopic strain and crystal rotation measurement within metallurgical grains, Key Eng. Mater. 592–593 (2014) 493–496. doi:10.4028/www.scientific.net/KEM.592-593.493.

[32] C. Schayes, J. Bouquerel, J.-B. Vogt, F. Palleschi, S. Zaefferer, A comparison of EBSD based strain indicators for the study of Fe-3Si steel subjected to cyclic loading, Mater. Charact. 115 (2016). doi:10.1016/j.matchar.2016.03.020.

[33] C. Schayes, J.-B. Vogt, J. Bouquerel, F. Palleschi, S. Zaefferer, Cyclic plasticity mechanism of the

M330-35A steel, Int. J. Fatigue. 82 (2016). doi:10.1016/j.ijfatigue.2015.09.008.

[34] C. Schayes, J.-B. Vogt, J. Bouquerel, F. Palleschi, Rotor Design Optimisation through Low Cycle Fatigue Testing, in: Procedia Eng., 2015. doi:10.1016/j.proeng.2015.12.663.

[35] M.F. De Campos, F.J.G. Landgraf, R. Takanohashi, F.C. Chagas, I.G.S. Falleiros, G.C. Fronzaglia, H. Kahn, Effect of the hot band grain size and intermediate annealing on the deformation and recrystallization textures in low silicon electrical steels, ISIJ Int. 44 (2004) 591–597. doi:10.2355/isijinternational.44.591.

[36] M.F. de Campos, F.J.G. Landgraf, I.G.S. Falleiros, G.C. Fronzaglia, H. Kahn, Texture Evolution during the Processing of Electrical Steels with 0.5% Si and 1.25% Si, ISIJ Int. 44 (2004) 1733–1737. doi:10.2355/isijinternational.44.1733.

[37] M.A. da Cunha, S. da C. Paolinelli, Low core loss non-oriented silicon steels, J. Magn. Magn. Mater. 320 (2008) 2485–2489. doi:10.1016/j.jmmm.2008.04.054.

[38] A. Ramazani, A. Schwedt, A. Aretz, U. Prahl, W. Bleck, Characterization and modelling of failure initiation in DP steel, Comput. Mater. Sci. 75 (2013) 35–44. doi:10.1016/j.commatsci.2013.04.001.

[39] N. McCormick, J. Lord, Digital image correlation, Mater. Today. 13 (2010) 52–54. doi:10.1016/S1369-7021(10)70235-2.

[40] Y. Chen, J. Hjelen, S.S. Gireesh, H.J. Roven, Optimization of EBSD parameters for ultra-fast characterization, J. Microsc. 245 (2012) 111–118. doi:10.1111/j.1365-2818.2011.03551.x.

[41] S.K. Paul, A critical review of experimental aspects inratcheting fatigue: Microstructure to specimen tocomponent, J. Mater. Res. Technol. 8 (2019) 4894–4914. doi:10.1016/j.jmrt.2019.06.014.

[42] H. Mughrabi, Dual role of deformation-induced geometrically necessary dislocations with

556 respect to lattice plane misorientations and/or long-range internal stresses, Acta Mater. 54
557 (2006) 3417–3427. doi:10.1016/j.actamat.2006.03.047.

558 [43] F. Ackermann, L.P. Kubin, J. Lepinoux, H. Mughrabi, The dependence of dislocation
559 microstructure on plastic strain amplitude in cyclically strained copper single crystals, Acta
560 Metall. 32 (1984) 715–725. doi:10.1016/0001-6160(84)90145-7.

561 [44] H. Mughrabi, K. Herz, X. Stark, Cyclic deformation and fatigue behaviour of alpha-iron mono-
562 and polycrystals, Int. J. Fract. 17 (1981) 193–220. doi:10.1007/BF00053520.

563 [45] D. Kuhlmann-Wilsdorf, C. Laird, Dislocation behavior in fatigue, Mater. Sci. Eng. 27 (1977)
564 137–156. doi:10.1016/0025-5416(77)90166-5.

565 [46] H. Mughrabi, Deformation-induced long-range internal stresses and lattice plane
566 misorientations and the role of geometrically necessary dislocations, Philos. Mag. 86 (2006)
567 4037–4054. doi:10.1080/14786430500509054.

568 [47] A. Irastorza-Landa, H. Van Swygenhoven, S. Van Petegem, N. Grilli, A. Bollhalder, S.
569 Brandstetter, D. Grolimund, Following dislocation patterning during fatigue, Acta Mater. 112
570 (2016) 184–193. doi:10.1016/j.actamat.2016.04.011.

571 [48] A. Irastorza-Landa, N. Grilli, H. Van Swygenhoven, Effect of pre-existing immobile dislocations
572 on the evolution of geometrically necessary dislocations during fatigue, Model. Simul. Mater.
573 Sci. Eng. 25 (2017). doi:10.1088/1361-651X/aa6e24.

574 [49] W. Pantleon, Resolving the geometrically necessary dislocation content by conventional
575 electron backscattering diffraction, Scr. Mater. 58 (2008) 994–997.
576 doi:10.1016/j.scriptamat.2008.01.050.

577 [50] J. Jiang, J. Yang, T. Zhang, F.P.E. Dunne, T. Ben Britton, On the mechanistic basis of fatigue
578 crack nucleation in Ni superalloy containing inclusions using high resolution electron
579 backscatter diffraction, Acta Mater. 97 (2015) 367–379. doi:10.1016/j.actamat.2015.06.035.

[51] J. Jiang, T.B. Britton, A.J. Wilkinson, Evolution of intragranular stresses and dislocation densities during cyclic deformation of polycrystalline copper, Acta Mater. 94 (2015) 193–204. doi:10.1016/j.actamat.2015.04.031.

[52] D. An, S. Zaefferer, Formation mechanism of dislocation patterns under low cycle fatigue of a high-manganese austenitic TRIP steel with dominating planar slip mode, Int. J. Plast. 121 (2019) 244–260. doi:10.1016/j.ijplas.2019.06.009.